



HAL
open science

PSO-based MPPT control of wind-driven Self-Excited Induction Generator for pumping system

Mohamed. Ali Zeddini, Remus Pusca, Anis Sakly, M. Faouzi Mimouni

► **To cite this version:**

Mohamed. Ali Zeddini, Remus Pusca, Anis Sakly, M. Faouzi Mimouni. PSO-based MPPT control of wind-driven Self-Excited Induction Generator for pumping system. *Renewable Energy*, 2016, 95, pp.162-177. <10.1016/j.renene.2016.04.008>. <hal-03673199>

HAL Id: hal-03673199

<https://univ-artois.hal.science/hal-03673199v1>

Submitted on 9 Jan 2024

HAL is a multi-disciplinary open access archive for the deposit and dissemination of scientific research documents, whether they are published or not. The documents may come from teaching and research institutions in France or abroad, or from public or private research centers.

L'archive ouverte pluridisciplinaire **HAL**, est destinée au dépôt et à la diffusion de documents scientifiques de niveau recherche, publiés ou non, émanant des établissements d'enseignement et de recherche français ou étrangers, des laboratoires publics ou privés.



HAL Authorization

1 PSO-based MPPT Control of Wind-driven Self-Excited 2 Induction Generator for Pumping System

3 Mohamed. Ali Zeddini ¹, Remus Pusca ², Anis Sakly ¹, M. Faouzi Mimouni ¹

4 (1) Research unit: Industrial Systems Study and Renewable Energy (ESIER), National Engineering School of Monastir
5 (ENIM), University of Monastir, Tunisia.

6 (2) Artois University, EA4025, Laboratory of Electrical Systems and Environment (LSEE), Bethune, F-62400, France.

7 zeddini_med_ali_enim@yahoo.fr

8 **Abstract**

9 In recent years, much research has been done to improve the performance of a wind energy conversion
10 system at various wind speeds using **Maximum Power Point Tracking (MPPT)** algorithms to find an
11 efficient production of peak energy.

12 In most cases, the MPPT techniques used to maximize the turbines power coefficient neglect the effect
13 of losses generated by the system components, which can shift the true optimal operating point of the
14 wind turbine. Furthermore, conventional MPPT methods such as **Perturbation and Observation (P&O)**
15 and **Incremental of Conductance (IncCond)**, need to sense both the rotor speed and the power of the
16 wind turbine. In addition, other methods such as Fuzzy Logic and neural networks based on MPPT
17 algorithms are proposed but these methods require knowledge of the wind speed and system parameters
18 for the training phase.

19 In this context, a new MPPT technique is being proposed in this paper, based on **Particle Swarm**
20 **Optimization (PSO)** for a standalone **Self-Excited Induction Generator (SEIG)** operating at variable
21 wind speed and supplying an induction motor coupled to a centrifugal pump.

22 **Keywords** - Self Excited Induction Generator, Pumping system, Maximum Power Point Tracking
23 Particle Swarm Optimization

25 **1. Introduction**

26 In the last decades, producing electricity with renewable energies such as wind and solar energy has
27 been considered to replace conventional resources [1-3]. Particularly, in remote site it is important to
28 limit the maintenance and to operate with minimum storage batteries, so the wind turbine pumping
29 systems without energy storage can be an alternative solution to conventional powered pumping
30 systems. In addition, this type of pumping systems does not pollute the environment.

31 Many types of generators are used for stand-alone power generation in remote site such as permanent
32 magnet, brushless, synchronous, asynchronous, variable reluctance. But the **Self Excited Induction**
33 **Generator (SEIG)** is mainly used because of its lower cost, high power density and very little
34 maintenance required [4-6].

35 During the last decades, several works have been developed to investigating a performance analysis of
36 the SEIG, and dynamic performance for feeding static and dynamic loads (resistive, inductive,
37 capacitive, and induction motor) at various wind speed conditions [7-10]. Therefore, the power
38 converter topology have been developed and various regulating schemes explored to obtain improved
39 voltage and frequency regulation [11,12]. In this scheme, the SEIG needs to control the providing
40 bidirectional flow of both active and reactive powers.

41 Other works have focused on architectures and methods for maximizing the wind power. Among them,
42 various regulating schemes have been adopted to extract the maximum power from the wind turbine
43 [13-15]. Consequently, the SEIG is operating at variable frequency, which needs a single power
44 controller. However, this scheme is gaining importance for stand-alone wind power applications, in
45 particular for water pumping systems with **Induction Motor (IM)** where the variation of the electrical
46 parameters is not very critical for its use.

47 Indeed, different control strategies referred to **Maximum Power Point Tracking (MPPT)** algorithms are
48 used to track peak power production efficiently at varying wind speeds. In this context, many techniques
49 of MPPT controller have been applied to induction generators such as, **Perturb and Observe (P&O)** or
50 Fuzzy logic, Neural network estimator [16-20]. The P&O technique is often proposed as solution for
51 MPPT controller for its simplicity calculus algorithm. The disadvantage of this technique is that it
52 introduces a continuous oscillation around the real maximum power point and have a limited ability to
53 track this point in the transient environmental conditions [16,17]. As a solution to improve the tracking
54 algorithm under speed-varying changes in wind speed, the Adaptive step Perturb and Observe strategy is
55 proposed in [18,19]. However, this technique which minimizes the oscillation needs to use the generator
56 rotor speed variation (as complementary information) to provide the correct direction to the **Maximum**
57 **Power Point (MPP)**.

58 Other MPPT strategies are implemented using intelligent computations like Artificial Neural Networks
59 [20] and Fuzzy logic [21, 22]. Recent improvements using a Fuzzy-Neuro based algorithm, combined
60 with an additional measurement of wind speed, obtain excellent precision in the tracking, but increase
61 the computational burden and cost.

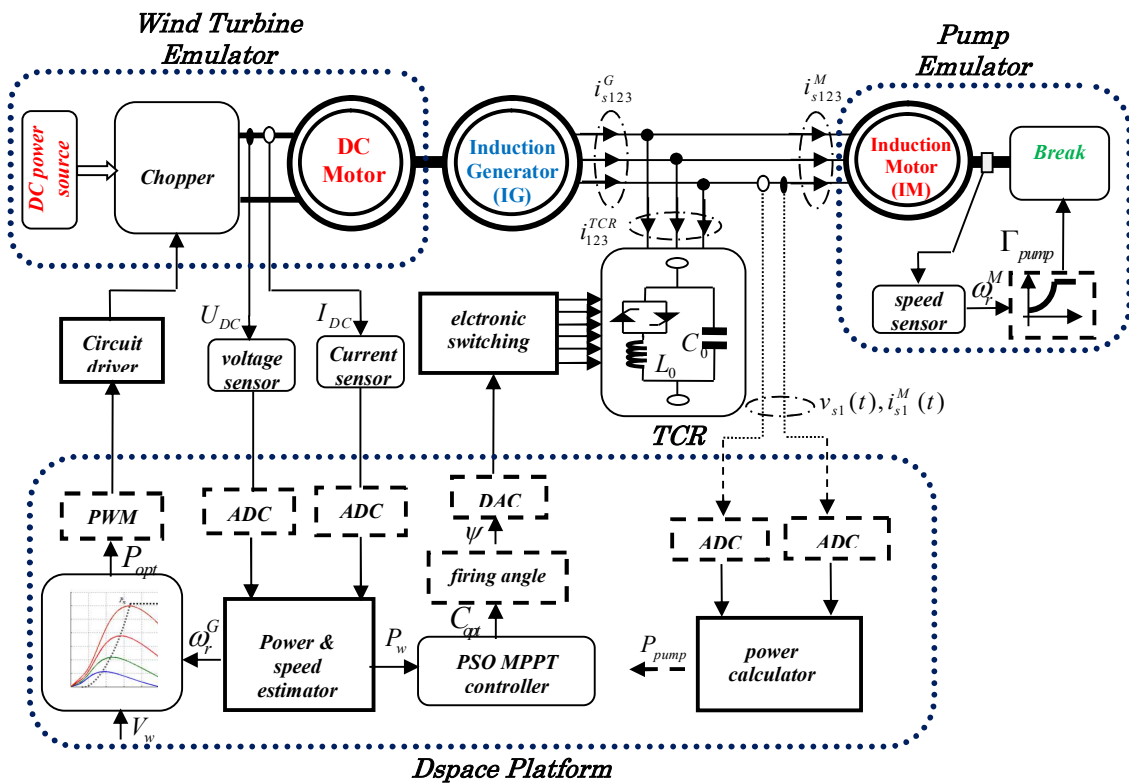
62 In this context, this paper presents a PSO-MPPT controller of wind-driven Self-Excited Induction
63 Generator for pumping systems which have not need to measure the wind or turbine speed. A SEIG-
64 Pump performance analysis is developed to extract the maximum power rated from the wind turbine.
65 The frequency is reached by using a **Thyristor Controller Reactor (TCR)** to adapt the rotor speed of the
66 SEIG at the desired value.

67 The whole paper is organized as follows: section 2 describes the dynamic modeling of the SEIG
68 pumping system, section 3 is devoted to presents the principle of MPPT control strategies. Simulation
69 results performed with Matlab/Simulink are discussed and presented in section 4. The location of the
70 MPP is calculated for different wind speed values to show the robustness and the efficiency of the

71 propose **PSO MPPT** algorithm. Experimental results are presented in section 5 with measurements on a
 72 test bench wind turbine emulator. Finally, a conclusion sums up the developed work and its features.

73 **2. Modeling of Wind Turbine Conversion System**

74 A wind turbine energy conversion system intended to work in isolated sites is shown in Fig.1. It
 75 consists of a DC Motor controlled through a chopper to emulate the wind turbine model used to convert
 76 wind kinetic energy , a squirrel cage **Induction Generator (IG)** to convert the mechanical power
 77 provided from the DC motor on electrical power, an induction motor which is coupled with a
 78 mechanical break to emulate the centrifugal pump model, a frequency controller based on Thyristor
 79 Controller Reactor system which is used to locate the MPP from the wind turbine, and a dSPACE
 80 controller board which is interfaced with a PC under Matlab/Simulink for the implementation of the
 81 PSO-MPPT controller .



82
 83 Fig .1. Schematic block diagram of the experimental test-bench of the wind turbine energy conversion
 84 system.

85 **2.1. Modeling of Wind Turbines Curve**

86 The power delivered by the wind turbine is proportional to the cube of the wind speed and can be
87 expressed as:

88
$$P_w = \frac{1}{2} \rho A V_w^3 \quad (1)$$

89 where ρ is the air density, A is the area swept by blades and V_w is the wind speed. A wind turbine can
90 only extract part of the power (maximum 59%) from the wind, which is given by the Betz limit [23].

91 Therefore, the wind turbine mechanical power extracted from the wind is given by:

92
$$P_m = \frac{1}{2} \rho A C_p(\beta, \lambda) V_w^3 \quad (2)$$

93 where $C_p(\lambda, \beta)$ is the power coefficient of the wind turbine. In this paper, the value of $C_p(\lambda, \beta)$ is
94 calculated as follows [24]:

95
$$C_p(\lambda, \beta) = 0.5179(116\lambda_i - 0.4\beta + 5)e^{-21\lambda_i} + 0.068\lambda \quad (3)$$

96 where the parameter λ_i is expressed as:

97
$$\lambda_i = \frac{1}{0.5/(\lambda + 0.08\beta) - 0.035/(\beta^2 + 1)} \quad (4)$$

98 The Tip Speed Ratio (TSR) is defined as the ratio between the blade tip speed and the wind speed:

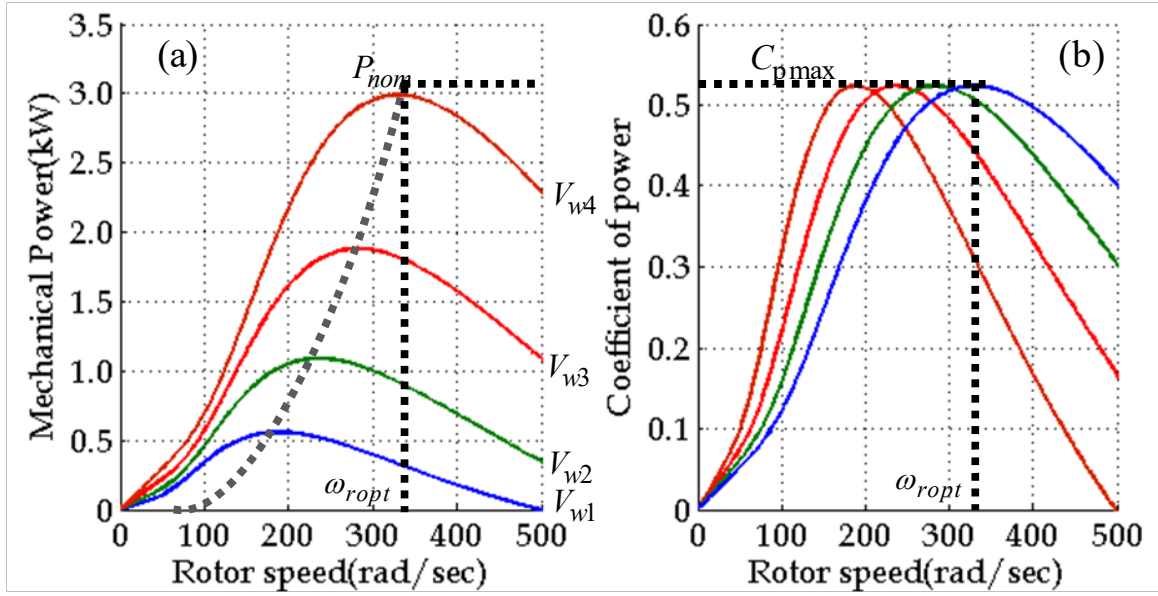
99
$$\lambda = \frac{R_w \Omega_r}{V_w} \quad (5)$$

100 where Ω_r denotes the rotor speed, and R_w is the radius of the wind turbine blade. The torque
101 developed by the wind turbine is given by:

102
$$\Gamma_w = \frac{P_m}{\Omega_r} = \frac{R_w}{2\lambda} \rho A V_w^2 C_p(\beta, \lambda) \quad (6)$$

103 β is the blade pitch angle, and λ is the Tip Speed Ratio.

104 Fig. 2 shows the power coefficient and the mechanical power curves of the wind turbine as a
105 function of the rotor speed for a pitch angle $\beta = 0^\circ$.



106

107 Fig. 2 Variation of (a) mechanical power curves and (b) power coefficient of the wind turbine for
 108 different wind speeds.

109 **2.2. Modeling of the Self Excited Induction Generator**

110 For the modeling and analysis of the SEIG, the stationary reference frame model is used. Moreover, the
 111 following differential equations describing the global generator model including the IG currents (

112 $i_{sd}^G, i_{sq}^G, i_{rd}^G, i_{rq}^G$) which integrated the auto-excitement capacitor C and the IM currents (i_{sd}^M, i_{sq}^M) are

113 developed as:

$$114 \quad \frac{d}{dt} \begin{pmatrix} i_{sd}^G \\ i_{sq}^G \\ i_{rd}^G \\ i_{rq}^G \\ v_{sd} \\ v_{sd} \end{pmatrix} = \frac{1}{D^G} \left\{ \begin{array}{cccccc} L_r^G R_s^G & -L_m^G \omega_r^G & -L_m^G R_r^G & -L_m^G L_r^G \omega_r^G & -L_r^G & 0 \\ L_m^G \omega_r^G & L_r^G R_s^G & L_m^G L_r^G \omega_r^G & -L_m^G R_r^G & 0 & -L_r^G \\ -L_m^G R_s^G & L_m^G L_s^G \omega_r^G & L_s^G R_r^G & L_s^G L_r^G \omega_r^G & L_m^G & 0 \\ -L_m^G L_s^G \omega_r^G & -L_m^G R_s^G & -L_s^G L_r^G \omega_r^G & L_s^G R_r^G & 0 & L_m^G \\ \frac{1}{C} & 0 & 0 & 0 & \frac{1}{C} & 0 \\ 0 & \frac{1}{C} & 0 & 0 & 0 & \frac{1}{C} \end{array} \right\} \begin{pmatrix} i_{sd}^G \\ i_{sq}^G \\ i_{rd}^G \\ i_{rq}^G \\ i_{sd}^M \\ i_{sq}^M \end{pmatrix} - \omega_r^G \begin{pmatrix} -L_m^G \\ -L_m^G \\ L_s^G \\ L_s^G \end{pmatrix} \phi_0 \quad (7)$$

115 where, $L_s^G = L_s^G + L_m^G$, $L_r^G = L_r^G + L_m^G$, and $D^G = L_m^G - L_s^G L_r^G$

116 R_s^G is the winding stator resistance, R_r^G the rotor resistance and ω_r^G the rotor speed of the wind

117 induction generator.

118 ϕ_0 is the remanant of the residual flux linkages, l_s^G the leakage inductance of the stator winding, l_r^G
 119 leakage inductance of the rotor copper arrangement referred to the stator, and L_m^G magnetizing
 120 inductance of the IG.

121 The electromagnetic torque developed by the IG can be computed in $d-q$ axes stator and rotor currents
 122 as:

$$123 \quad \Gamma_{em}^G = \frac{3}{2} \left(\frac{P}{2} \right) [i_{rd}^G i_{sq}^G - i_{sd}^G i_{rq}^G] \quad (8)$$

124 The equation which represents the SEIG mechanical behavior will be assumed to be expressible as:

$$125 \quad \begin{cases} J \frac{d\Omega_r^G}{dt} + \Gamma_f = \Gamma_\omega - \Gamma_{em}^G \\ \Gamma_\omega = \frac{P_w}{\Omega_r^G} \end{cases} \quad (9)$$

126 where Γ_ω represents the torque which acts on the SEIG shaft by means of the blades, Γ_f is the friction
 127 torque, P_w is the corresponding mechanical power and J is the global inertia of the system.

128 2.3. Model of the Induction Motor

129 The differential equations describing the stator currents (i_{sd}^M , i_{sq}^M) and rotor currents (i_{rd}^M and i_{rq}^M) of
 130 the IM using a $d-q$ components of stator voltage (v_{sd} and v_{sq}) are developed as:

$$131 \quad \frac{d}{dt} \begin{pmatrix} i_{sd}^M \\ i_{sq}^M \\ i_{rd}^M \\ i_{rq}^M \end{pmatrix} = \frac{1}{D^M} \begin{bmatrix} -pL_m^M \Omega_r^M & -L_r^M r_s^M & -pL_m^M L_r^M \Omega_r^M & -L_m^M r_r^M \\ -L_r^M r_s^M & pL_m^M \Omega_r^M & -L_m^M r_r^M & pL_m^M L_r^M \Omega_r^M \\ pL_m^M L_s^M \Omega_r^M & L_m^M r_s^M & pL_s^M L_r^M \Omega_r^M & L_s^M r_r^M \\ L_m^M r_s^M & -pL_m^M L_s^M \Omega_r^M & L_s^M r_r^M & pL_s^M L_r^M \Omega_r^M \end{bmatrix} \begin{pmatrix} i_{sd}^M \\ i_{sq}^M \\ i_{rd}^M \\ i_{rq}^M \end{pmatrix} + \frac{1}{D^M} \begin{bmatrix} -L_r^M & 0 \\ 0 & -L_r^M \\ L_m^M & 0 \\ 0 & L_m^M \end{bmatrix} \begin{pmatrix} v_{sd} \\ v_{sq} \end{pmatrix} \quad (10)$$

132 where, $L_s^M = l_s^M + L_m^M$, $L_r^M = l_r^M + L_m^M$ and $D^M = L_m^M - L_s^M L_r^M$,

133 l_s^M is the leakage inductance of the stator winding, l_r^M leakage inductance of the rotor copper
 134 arrangement referred to the stator and p is the pair of poles. r_s^M is the winding stator resistance, r_r^M
 135 the rotor resistance and ω_r^M the rotor speed of the induction motor.

136 The electromagnetic torque of the IM can be computed in $d-q$ axes stator and rotor currents as:

137
$$\Gamma_{em}^M = \frac{3}{2} \left(\frac{p}{2} \right) [i_{rd}^M i_{sq}^M - i_{sd}^M i_{rq}^M] \quad (11)$$

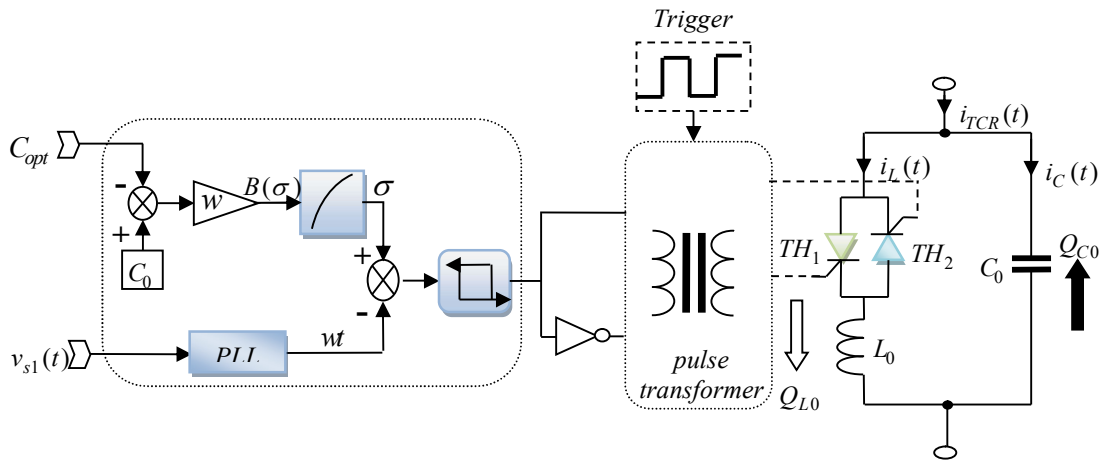
138 The equation which represents the IM mechanical behavior will be expressible as:

139
$$\begin{cases} J \frac{d\Omega_r^M}{dt} + \Gamma_f = \Gamma_{em}^G - \Gamma_{pump} \\ \Gamma_{pump} = \frac{P_{pump}}{\Omega_r^M} = k_n \Omega_r^M \end{cases} \quad (12)$$

140 with k_n and P_{pump} electrical pump power

141 **2.4. Modeling of the TCR System**

142 A Thyristor Controlled Reactor circuit is basically composed of two oppositely poled thyristors and
 143 a reactor [25,8]. The reactor is composed as two elements; a relatively big fixed capacitor $C_0 = 75 \mu F$
 144 and a fixed self inductance $L_0 = 335 \text{ mH}$. A per phase circuit of TCR circuit is shown in Fig. 3.



145
 146 Fig. 3. Per phase equivalent circuit of TCR system and open loop control scheme for frequency
 147 regulation.

148 The instantaneous current absorbed by the self inductance L_0 is given by:

$$149 \quad i_{L_0} = \begin{cases} \frac{V_s}{\pi L_0 \omega} \sqrt{2} [\cos(\psi) - \cos(\omega.t)] & \psi < \omega.t < \psi + \sigma \\ 0 & \psi + \sigma < \omega.t < \pi \end{cases} \quad (13)$$

150 where σ is the thyristor conduction angle, and ψ is the thyristor firing angle.

151 V_s and ω are the RMS and the frequency of the SEIG terminal voltage respectively.

152 The fundamental component is found by Fourier analysis, and is given by:

$$153 \quad I_1 = \frac{\sigma - \sin(\sigma)}{\pi L_0 \omega} V_s = B(\sigma) V_s \quad (14)$$

154 where $B(\sigma)$ is an adjustable fundamental frequency susceptance.

155 The TCR system is controlled by adjusting a fundamental frequency susceptance whose reactive
156 power is balanced according to the requirement current in the SEIG. However, the reactive power Q_{TCR}
157 generated by a TCR system is equal to the difference between the capacitor power Q_{C_0} and the
158 inductance power Q_L as:

$$159 \quad Q_{TCR} = Q_{C_0} - Q_{L_0} = 3(C_0 \omega - B(\sigma)) V_s^2 \quad (15)$$

160 The generated firing pulses for the thyristors are obtained by a pulse transformer and a trigger which
161 is synchronized with the line voltages using a PLL system.

162 **3. Analysis of the Proposed MPPT Controller**

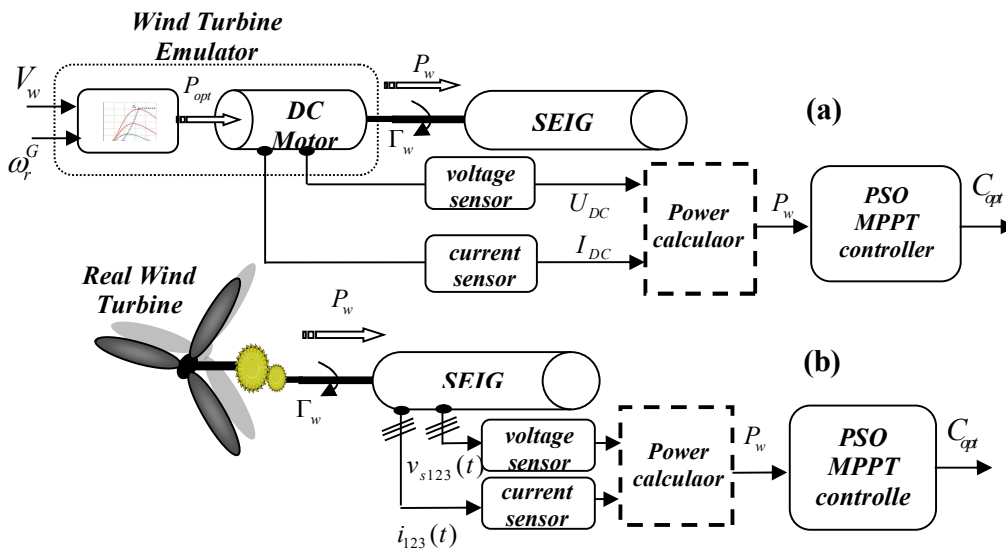
163 **3.1. MPPT Controller Principle**

164 Considering the mechanical power curves presented in Fig. 2.a we can note that the power of a wind
165 turbine is maximum for a rotor speed called optimum rotor speed ω_{ropt} . So in order to extract maximum

166 possible power, the wind turbine should be operated at this speed. During the constant wind speed is
 167 possible to control the rotational speed of the wind turbine by changing the reactive power.

168 Note that the operating slip of the induction generator is a small value. Therefore, for operating at
 169 **Maximum Power Point (MPP)**, the rotor speed can be controlled by adjusting the capacitor value which
 170 also influences the frequency value of the SEIG. In a classical P&O algorithm, the MPP can be obtained
 171 by measuring two parameters: electrical power (P_w) and rotor speed ω_r . The particularity of the
 172 proposed PSO algorithm is that it uses only electrical power (P_w) parameter as reference to estimate the
 173 optimal value of the capacitor which leads to ω_{opt} .

174 For the wind turbine emulation, the proposed PSO-MPPT controller is based on measurement of
 175 electrical variables (U_{DC} and I_{DC}) as is shown in Fig. 4a. In a real wind turbine, the measurement of the
 176 mechanical power is complex or not always available. So it is possible to maximize the electrical power
 177 extracted from the SEIG considering the measured power at the SEIG output as the image of the
 178 mechanical power at the SEIG shaft. This case is shown in Fig. 4b and proposed in the presented PSO
 179 algorithm.



180
 181 Fig. 4. Schematic diagram of power estimation: a) wind emulator and power estimation using DC motor
 182 electrical signals b) power estimation using SEIG electrical signals.

183
184 In this case the losses are considered constants and the maxima values of electrical and mechanical
185 powers obtained having the same optimal rotor speed value ω_{opt} .

186 For experimental bench a realistic wind turbine curve and a rotor speed estimator are used to calculate
187 the optimal reference mechanical power P_{opt} for the DC motor. It will be controlled under a PWM
188 chopper to generate the corresponding mechanical power P_w to the SEIG shaft.

189 In the proposed PSO algorithm, as the rotor speed ω_r can be modified by changing the capacity value, a
190 vector of capacitor C_j^k is used as initial value. j is the index of evolving parameters ($j = 1, 2, \dots, N_p$) called
191 particles and their values change at each iteration k . For each iteration, these j values of the capacity are
192 sent to the TCR system, which imposes to the SEIG a frequency f_j^k and a rotor speed ω_{rj}^k . The wind
193 turbine emulator use a characteristic wind curve memorized in a look-up table and a rotor speed
194 estimator to calculate P_{opt} . In the test bench is used a power loop control for DC motor under a PWM
195 chopper to generate the corresponding mechanical power to the SEIG shaft. After the sending of the first
196 capacity value C_j^k and the establishment of the permanent regime of mechanical and electrical
197 quantities in the generator, voltage and current sensors are used to measure the electrical power and to
198 estimate the mechanical power (P_{wj}^k) applied at the SEIG shaft. In the same iteration k the TCR system
199 receives the second reference of the capacity value C_{j+1}^k , which imposes to the DC machine a new
200 mechanical shaft power P_{wj+1}^k . The last value of the capacity for the iteration k is $C_{N_p}^k$. Each time
201 necessary to establish the permanent regime and to measure electrical variables (U_{DC} and I_{DC}) for C_j^k
202 depends on the global inertia system, parameters of the SEIG and requires for presented system

203 approximately 200 ms. For practical implementation the number of particles N_p must be limited (
 204 $N_p \leq 4$). In presented application the global iteration time is near to 800 ms and this cycle will be
 205 repeated continuously until the real mechanical power achieves the maximum power points (MPP) . It
 206 can be noticed in Fig.4.b that for a real wind turbine the proposed PSO algorithm does not need to
 207 measure or estimate the rotor speed.

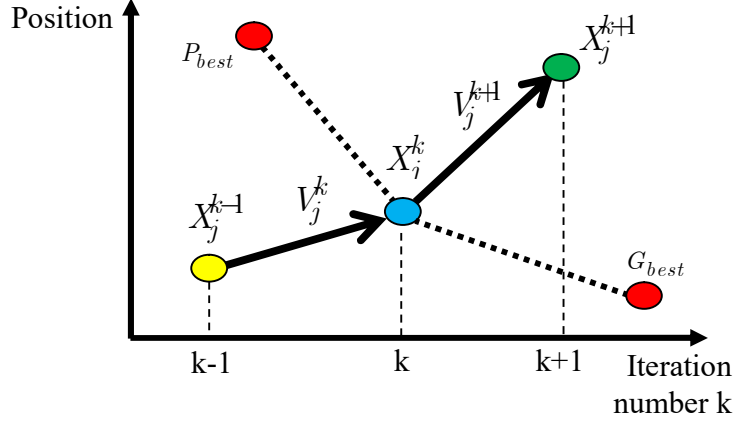
208 3.2. PSO Overview

209 The Particle Swarm Optimization (**PSO**) is a population-based searching algorithm. In general cases,
 210 it randomly produces N_p particles in searching space, where each particle is characterized by a position
 211 X_j^k in the searching space, and a velocity V_j^k [26, 28]. Each position of particle $X_j^{(k)}$ (in this case the
 212 capacity C_j^k) represents a solution of the problem and the "velocity" $V_j^{(k)}$ its displacement (variation of
 213 ΔC_j^k) in the searching space (between C_{\min} and C_{\max}). The particles have memory to keeps track of
 214 its previous best particle called P_{best} which corresponds to an optimal fitness function Fit_{opt} (a
 215 mathematical function where the objective is to be minimized by changing the particles) obtained for
 216 iteration k. After the second iteration (k+1) is memorized (between P_{best_k} and $P_{best_{k+1}}$), the particle gives
 217 the minimized value of the Fit_{opt} . This particle (capacity in presented application) is called G_{best} . This
 218 concept considers a random weighted acceleration at each time step [28]:

$$219 \begin{cases} V_j^{(k+1)} = \mu V_j^{(k)} + \delta_1 rand[0,1](P_{best} - X_j^{(k)}) + \delta_2 rand[0,1](G_{best} - X_j^{(k)}) \\ X_j^{(k+1)} = X_j^{(k)} + V_j^{(k+1)} \end{cases} \quad (16)$$

220 where, $j = 1, 2, \dots, N_p$ is the index of particles, μ is the momentum or inertia ($\mu = 0.5$), δ_1 and δ_2 are a
 221 positive constant ($\delta_1 = \delta_2 = 0.5$), $rand$ is random numbers which are uniformly distributed in $[0, 1]$,

222 and k is the iteration number. A typical movement of particles in the optimization process is shown in
 223 Fig. 5.



224

225 Fig. 5. Typical movement of particles in the searching space or optimization process.

226 In this figure the general spatial evolution case (between two iterations k , and $k+1$) of particles $X_j^{(k)}$ to
 227 $X_j^{(k+1)}$ is presented. It takes in consideration the velocity evolution from V_j^k to V_j^{k+1} . The best $X_j^{(k)}$
 228 value for the j particles which give a minimal value for Fit function at iteration k is memorized with
 229 the name P_{best} (local best value) and the best value between all realized iterations is memorized with the
 230 name G_{best} (global best value). In the presented PSO algorithm a scalar particles evolution is considered
 231 where the particles are capacity values ($C_1^{(k)}, C_2^{(k)}, C_3^{(k)}, C_4^{(k)} \dots$) and the velocity evolution are the
 232 capacity variation $\Delta C_1^k, \Delta C_2^k, \Delta C_3^k, \Delta C_4^k \dots$.

233 3.3. Application of PSO Algorithm for MPPT

234 In this paper, the initial N_p particles ($N_p = 4$) are chosen to be uniformly distributed between C_{min} and
 235 C_{max} . So, the value of particles and the corresponding velocity at the first iteration ($k=1$) are defined as:

$$236 \quad X_j^{(k)} = V_j^{(k)} = C_j^k = \frac{C_{max} - C_{min}}{N_p - 1} (j - 1) + C_{min} \quad (17)$$

$$237 \quad j = 1, 2, \dots, N_p$$

238 where, for the presented algorithm, $C_{\min} = 35\mu F$ and $C_{\max} = 110\mu F$ are the low bound and the upper
 239 bound values of the optimal capacitor C_{opt} . The objective of the PSO algorithm is to maximize the
 240 generated power of the wind turbine ($P_w(C_j^{(k+1)}) > P_w(C_j^{(k)})$) consequently to minimize the fitness
 241 function Fit described by the following equation:

$$242 \quad Fit = \min \Delta P = |P_{nom} - P_w(C_j^k)| \quad (18)$$

243 The updating of the particles $C_j^{(k)}$ and each capacity variation $\Delta C_j^{(k)}$, are given by the following
 244 equation [26]:

$$245 \quad \begin{cases} \Delta C_j^{(k+1)} = \mu \Delta C_j^{(k)} + \delta_1 rand[0,1](C_{jPbest}^k - C_j^{(k)}) + \delta_2 rand[0,1](C_{jGbest}^k - C_j^{(k)}) \\ C_j^{(k+1)} = C_j^{(k)} + \Delta C_j^{(k+1)} \end{cases} \quad (19)$$

246 where, C_{jPbest}^k and C_{jGbest}^k are the local and global best capacity solution which lead to a minimal value
 247 of the Fit . The best local capacity solution is obtained using the following relationship:

$$248 \quad C_{jPbest}^k = \begin{cases} C_j^k & \text{for } P_w(C_j^{(k)}) > P_w(C_{j-1}^{(k)}) \\ C_{j-1}^k & \text{for } P_w(C_j^{(k)}) < P_w(C_{j-1}^{(k)}) \end{cases} \quad (20)$$

249 At latest iteration k the best local power is obtained for the best capacity value:

$$250 \quad P_w^k = P(C_{jPbest}^k) \quad (21)$$

251 For the global best capacity solution, considering all realized iterations C_{jGbest}^k is defined by the best
 252 solution under latest and previous iteration. It is given as:

$$253 \quad C_{jGbest}^k = \begin{cases} C_{jPbest}^k & \text{for } P_w(C_{jPbest}^{(k)}) > P_w(C_{jPbest}^{(k-1)}) \\ C_{jPbest}^{k-1} & \text{for } P_w(C_{jPbest}^{(k-1)}) > P_w(C_{jPbest}^{(k)}) \end{cases} \quad (22)$$

254 This capacity C_{jGbest}^k gives the minimal value for fitness function at iteration k and it makes it possible to
 255 extract more power from the wind turbine. We note that, in order to avoid the disconnection of the

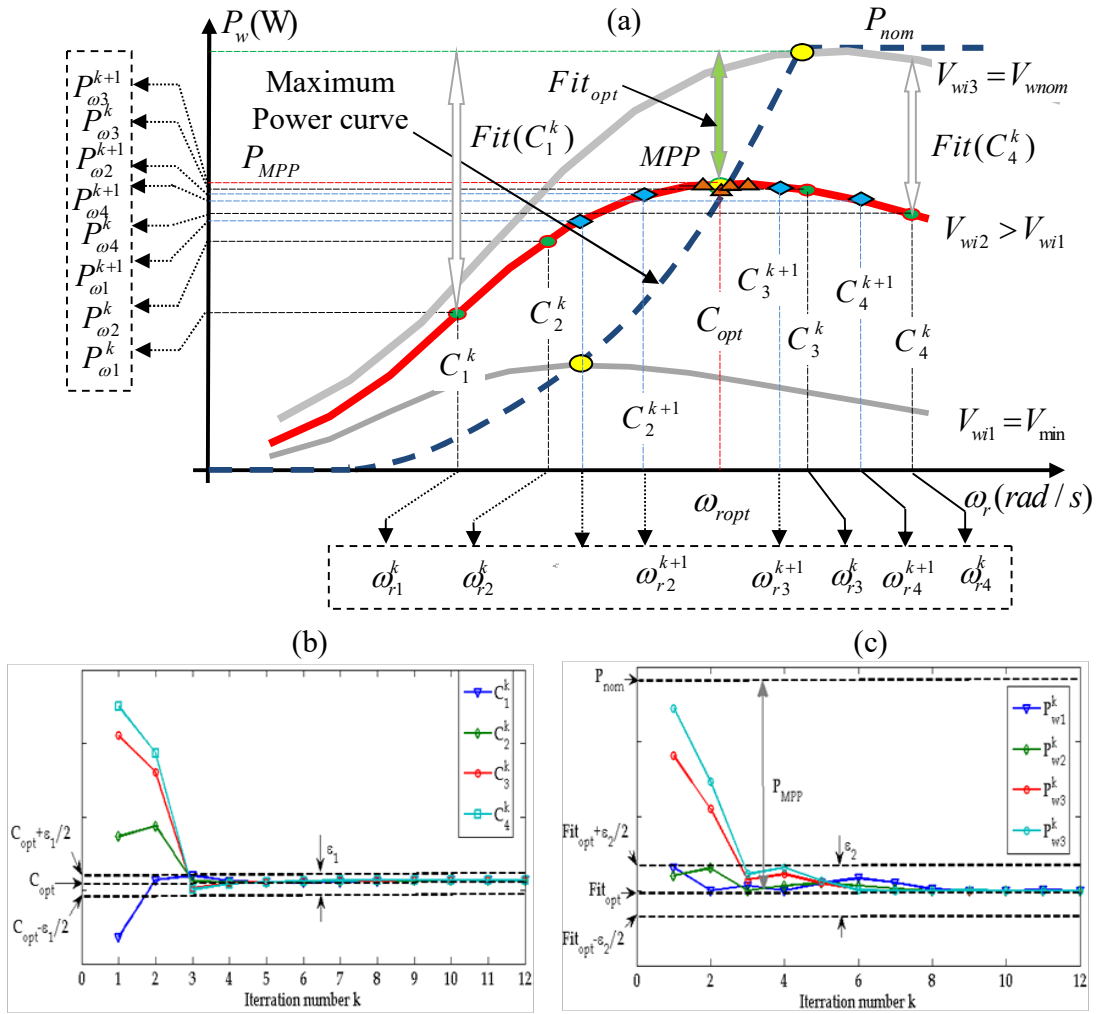
256 SEIG, limitations of the capacity value must be imposed ($C_{\min} < C_j^k < C_{\max}$). Taking this constraint into
 257 consideration the new capacity can be expressed by:

$$258 \quad C_j^{k+1} = \begin{cases} C_{\min} & \text{for } C_j^{(k)} + \Delta C_j^{(k+1)} < C_{\min} \\ C_j^{(k)} + \Delta C_j^{(k+1)} & \text{for } C_{\min} < C_j^{(k)} + \Delta C_j^{(k+1)} < C_{\max} \\ C_{\max} & \text{for } C_j^{(k)} + \Delta C_j^{(k+1)} > C_{\max} \end{cases} \quad (23)$$

259 Fig.6.a illustrates the application of the PSO algorithm in tracking the MPP, using a first vector of
 260 capacitor with four particles. To start the optimization process (iteration k), the algorithm transmits to
 261 the TCR system four capacitor reference values ($C_1^k, C_2^k, C_3^k, C_4^k$). The number of the particles must be
 262 correlated with the system inertia and in this application limited to $N_p=4$. In Fig. 6.a, the four initial
 263 particles are marked with circular points and for each point there is one capacitor value. Each capacitor
 264 imposes a rotor speed ($\omega_{r1}^k, \omega_{r2}^k, \omega_{r3}^k, \omega_{r4}^k$) which corresponds to a mechanical power ($P_{w1}^k, P_{w2}^k, P_{w3}^k, P_{w4}^k$).
 265 We can notice here that C_3^k is the best particle in the first iteration k, which gives the best power value ($P_{best} = P_{w3}^k$), corresponding to maximum mechanical power at the first iteration.

267 For the second iteration (iteration k+1), the particle updating is realized using equation 17. It is
 268 calculated new capacitor vector $C_1^{k+1}, C_2^{k+1}, C_3^{k+1}, C_4^{k+1}$. These new particles are marked with square points
 269 in Fig. 6.a. A new best personal particle C_3^{k+1} is found and the best power is obtained at P_{w3}^{k+1} , which
 270 corresponds to best rotor speed ω_{r3}^{k+1} . In fact, it is a global best ($C_{Gbest} = C_3^{k+1}$), which represents the best
 271 particles between the latest and the previous iterations corresponding to the greater best power P_{w3}^{k+1} .

272 In the third iteration (iteration k+2), all capacitor particles ($C_1^{k+2}, C_2^{k+2}, C_3^{k+2}, C_4^{k+2}$) come near to MPP. In
 273 the subsequent iteration, due to very low velocity, the value of the rotor speed ($\omega_{r1}^{k+2}, \omega_{r2}^{k+2}, \omega_{r3}^{k+2}, \omega_{r4}^{k+2}$) is
 274 approaching to optimal rotor speed ω_{ropt} . Therefore, the wind turbine power will be maintained at the
 275 maximum power (P_{MPP}), and the oscillation around it diminishes.



276

277 **F** Fig. 6. Curves of a) MPP evolution on the wind turbine power, b) capacity and c) fitness optimization.

278 This sequence will be repeated continuously until the particles gradually come close to achieving MPP.

279 This algorithm is realized during a constant wind speed. Fig. 6.b and Fig.6.c present the evolution of the

280 capacity and fitness function for different iteration numbers. We can notice that after $k=3$ iterations the

281 Fit is minimized and the turbine works at MPP. The time necessary to detect the MPP is dependent on

282 the global system inertia of the machine. In presented test bench, the global time to detect the new MPP

283 is estimated at approximately 2.4s (4×200 ms $\times 3$). If the wind speed applied changes the PSO algorithm

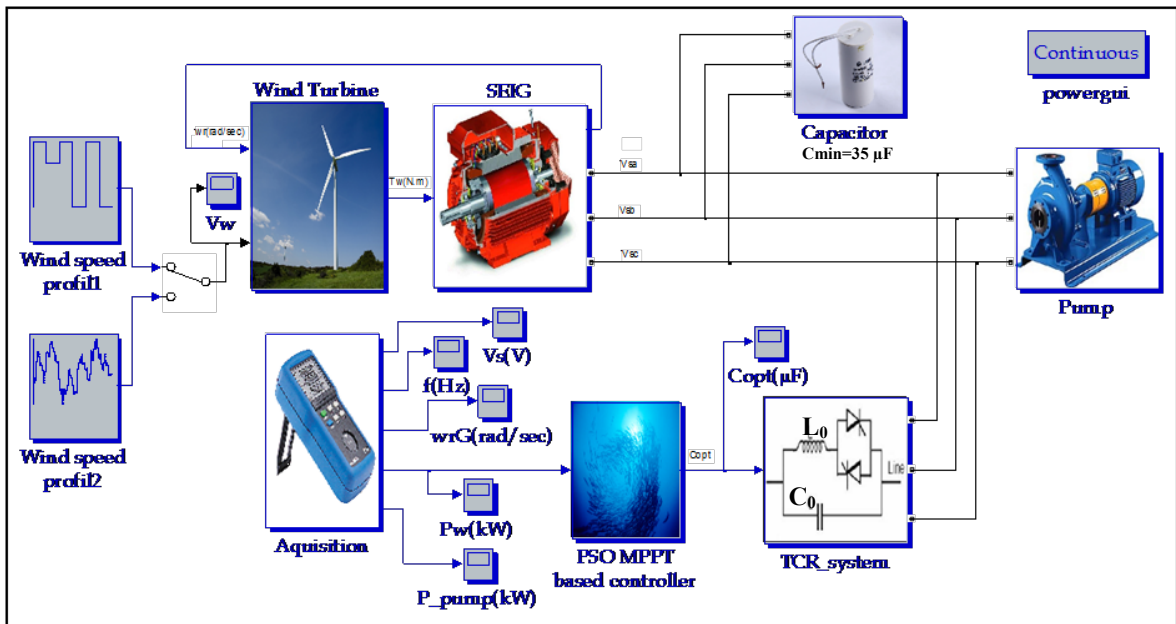
284 must be reinitialized automatically to search again a new maximal power point. In this case two

285 following simultaneous conditions must be respected to reinitialize the MPPT controller:

296 **4. Simulation Results and Discussion**

297 The simulations are carried out using Matlab/Simulink mathematical analysis software package. The
 298 system component parameters are presented in Appendix 1.

299 A TCR system composed of a fixed big capacitor $C_0 = 75\mu F$ and a fixed big inductance $L_0 = 335mH$
 300 is used, whose principle is to adjust SEIG rotational speeds according to an optimal reference speed
 301 obtained from an MPPT controller. The simulink program begins with small initial voltage in the d and
 302 q axes of the stator due to residual magnetism. The block diagram of the global simulated system is
 303 shown in Fig. 8.



304
 305 Fig. 8. Global simulink model for the wind turbine energy conversion system.

306 Initially, the SEIG start up process without pump, until the priming of the SEIG is reached. During this
 307 time, we hang the pump and the regulation system. Simulation was carried out for two wind speed
 308 profiles applied to the wind turbine, incorporating the proposed MPPT controller.

309 However, to validate the dynamic performance of the proposed MPPT controller, a step wind speed
 310 profile shown in Fig. 9 was applied to the wind turbine. In this case, the wind speed has been changed

311 from 13 m/s to 12 m/s and back to 13 m/s. The wind profile was to be changed again from 10 m/s to 13
312 m/s and back to 10 m/s.

313 The simulated waveforms of optimal capacitor, (C_{opt}), Fig. 10, rotor speed (ω_r^G) Fig. 11, shaft
314 power of wind turbine (P_w) Fig. 12 and pump (P_{pump}), wind turbine curve $f(P_w, \omega_r^G)$ Fig. 13
315 terminal RMS phase voltage (U_s) and frequency(f) Fig. 14 are presented for the step change of the
316 wind speed (V_w). It can be seen from Fig. 11 that the real rotor speed (ω_r^G) is converged to the optimal
317 rotor speed ($\omega_{r_{opt}}^G$) obtains by the PSO MPPT algorithm. Furthermore, the wind turbine power (P_w) is
318 maintained at the maximum power (P_{MPP}). In fact, the proposed MPPT controller has managed to track
319 the MPP for different values of wind speed (Fig. 13).

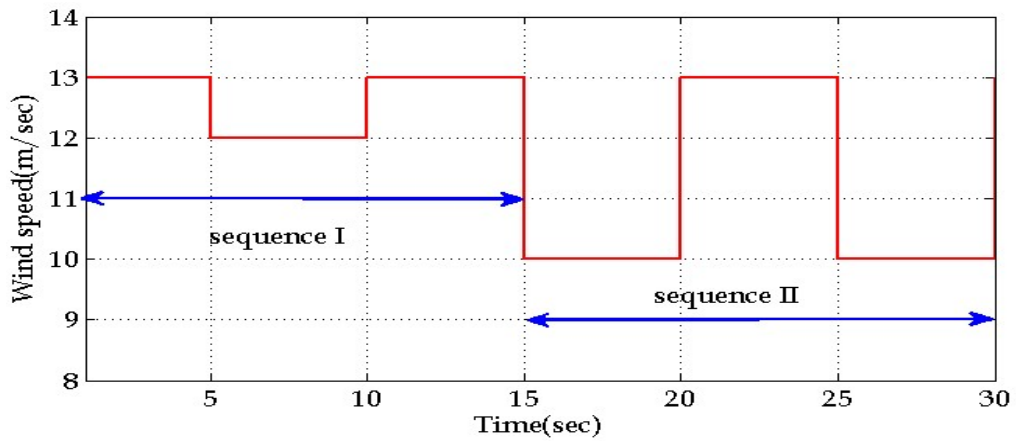
320 To observe the performance of the proposed MPPT algorithm, the instantaneous wave forms of the
321 first line voltage of the SEIG and those of the TCR system is shown and zoomed in Fig.15.

322 In Fig.16 the first line currents of the I_{SEIG} , the first line current I_{TCR} of the TCR system and those of
323 the pump are shown. We can notice that the I_{TCR} changing during each considered interval ($V_w=12\text{m/s}$,
324 $V_w=10\text{m/s}$, $V_w=13\text{m/s}$) when the reactive power is changed and so the ω_r , respectively the frequency.

325 Furthermore, to assess the successful working of the proposed MPPT controller for a large value of
326 wind speed, a more realistic wind speed profile illustrated in Fig.17 was applied to the wind turbine.
327 Simulation results represent the optimal capacitor variation (C_{opt}). Fig. 18, the rotor speed (ω_r^G), Fig.
328 19 the active power of wind turbine (P_w), pump (P_{pump}), estimation power by MPP algorithm P_{MPP} , Fig.
329 20, terminal RMS voltage (U_s) and frequency (f) Fig. 21, gives the time evolution of presented
330 parameters.

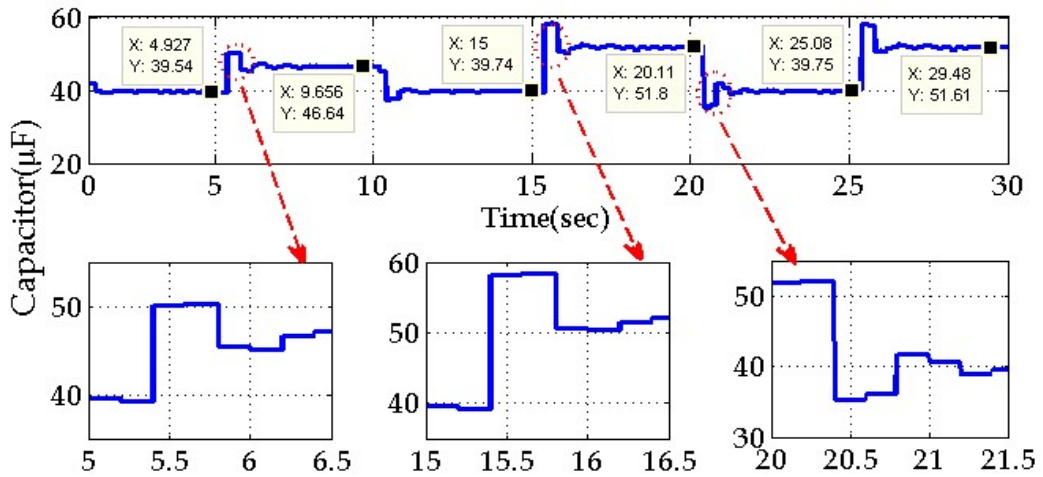
331 It can be seen from this figure that the maximum value of power of the turbine (P_w) shown in Fig.12
 332 is already reached, and it was equal to the MPP power found by the MPPT controller. It can therefore be
 333 observed from the simulation results a good tracking capability of the proposed MPPT controller.

334 The first and the second test involve increasing or decreasing the reference speed keeping the torque
 335 constant. The aim of this case is to evaluate the performance of the proposed PSO-MPPT controller.



336

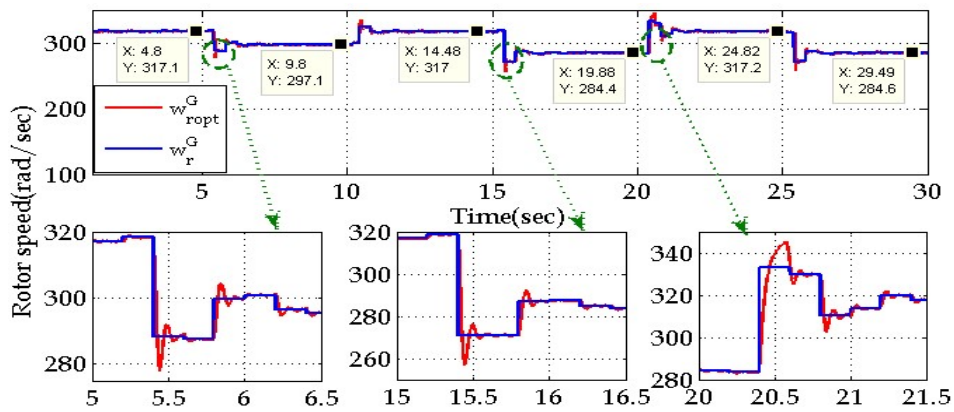
337 Fig . 9. Step wind speed profile for simulation tests.



338

339 Fig. 10. Variations of optimal capacitor during step wind speed variation; $V=13\text{m/s}$ and $V=12\text{m/s}$.

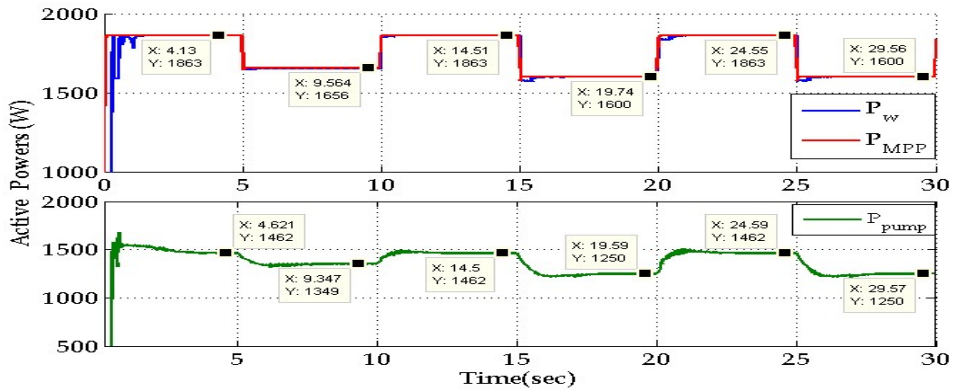
340



341

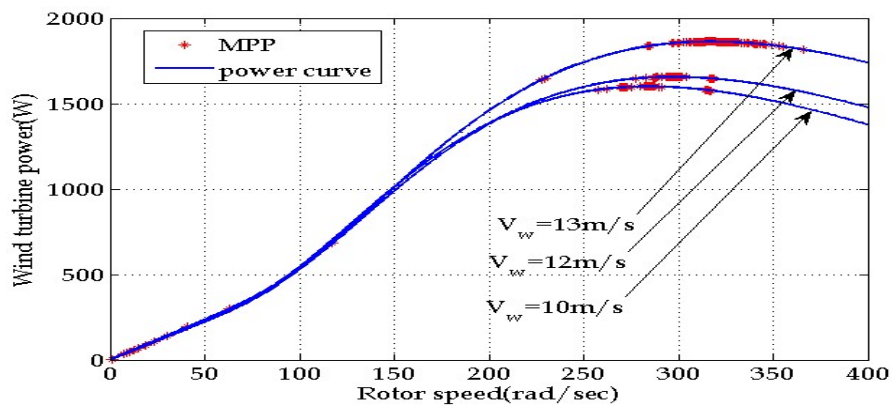
342 Fig. 11. Variations of optimal rotor speed and measured rotor speed during wind speed variation.

343



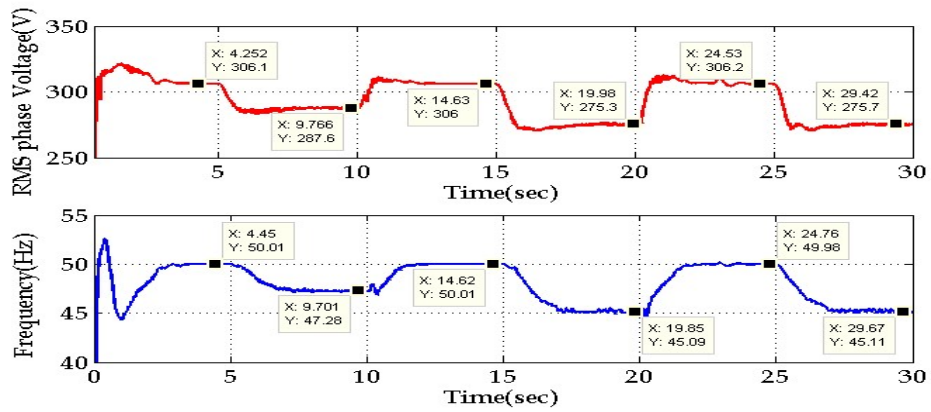
344

345 Fig. 12. Variations of active power of wind turbine P_w , active power of pump P_{pump} and estimated power
346 P_{MPP} during wind speed step variation.



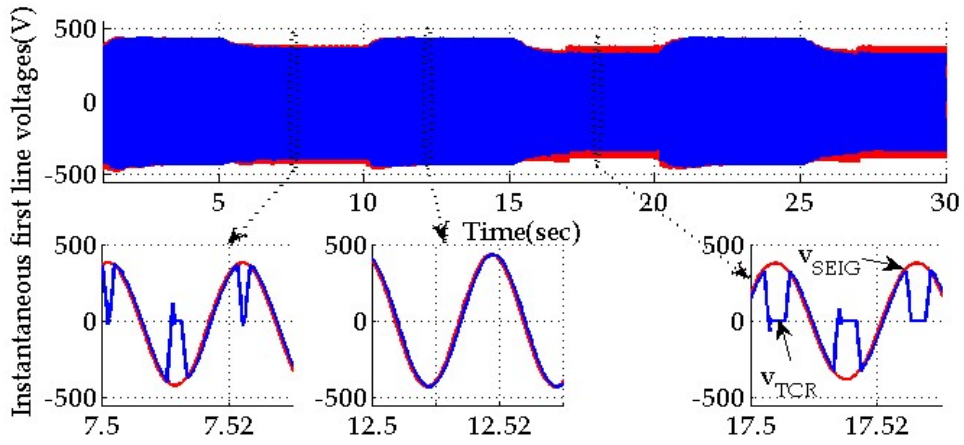
347

348 Fig. 13. Mechanical power of wind turbine characteristics and estimated power by MPP algorithm.



349

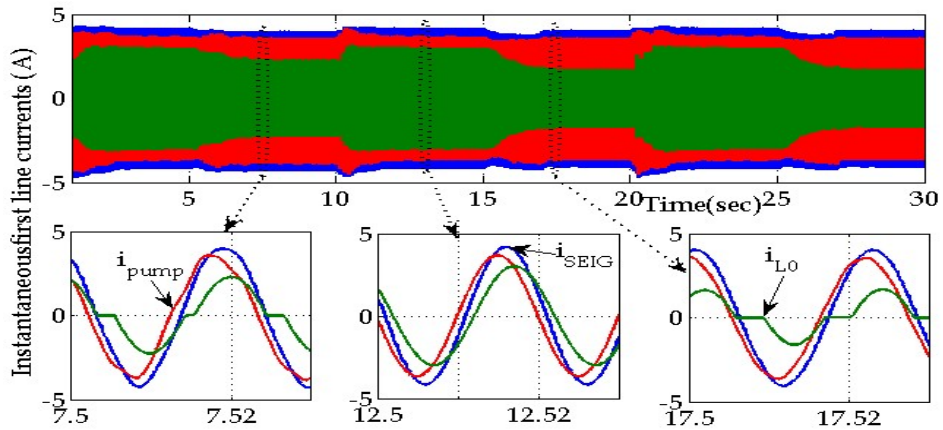
350 Fig. 14. Variations in RMS phase line voltage and frequency of the SEIG during wind speed step
 351 variation.



352

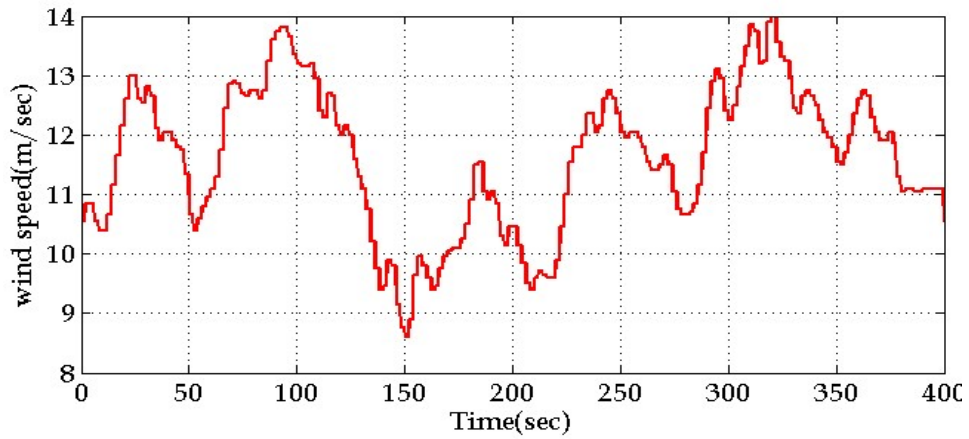
353 Fig. 15. Instantaneous first line voltage of the SEIG and TCR system during wind speed step
 354 variation.

355

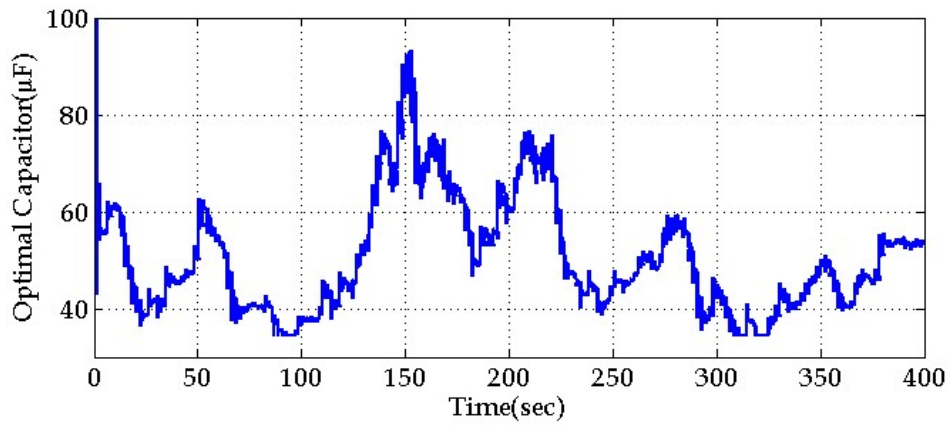


356

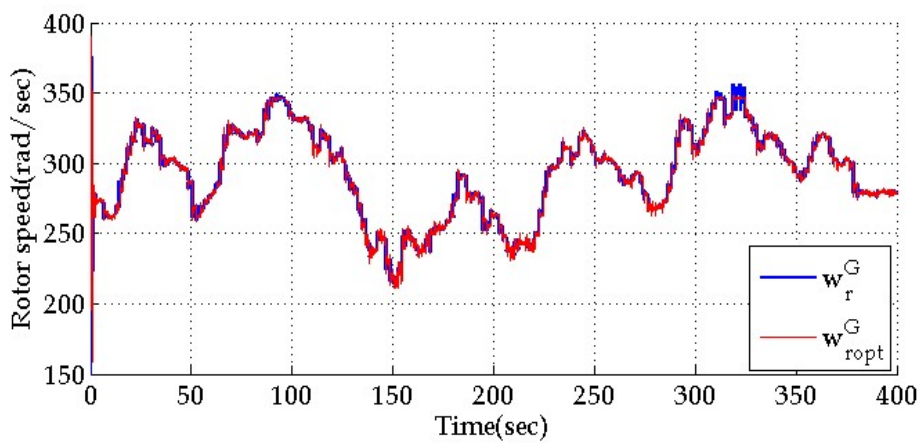
357 Fig. 16. Instantaneous first line currents of a) SEIG, b) TCR system and c) IM (pump) under wind
 358 speed perturbations.



359
 360 Fig. 17. Realistic wind speed profile used in the second simulation tests.

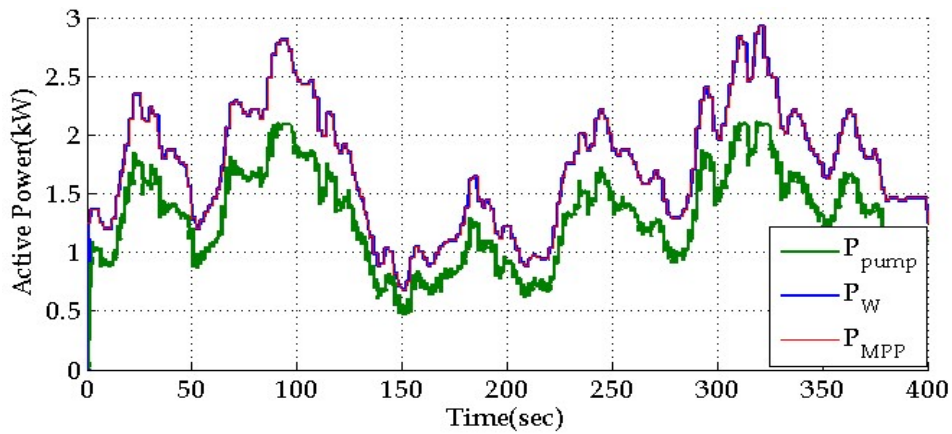


361
 362 Fig. 18. Variations of optimal capacitor during wind speed variation.



364
 365 Fig. 19. Variations of optimal rotor speed and measured rotor speed during wind speed variation.

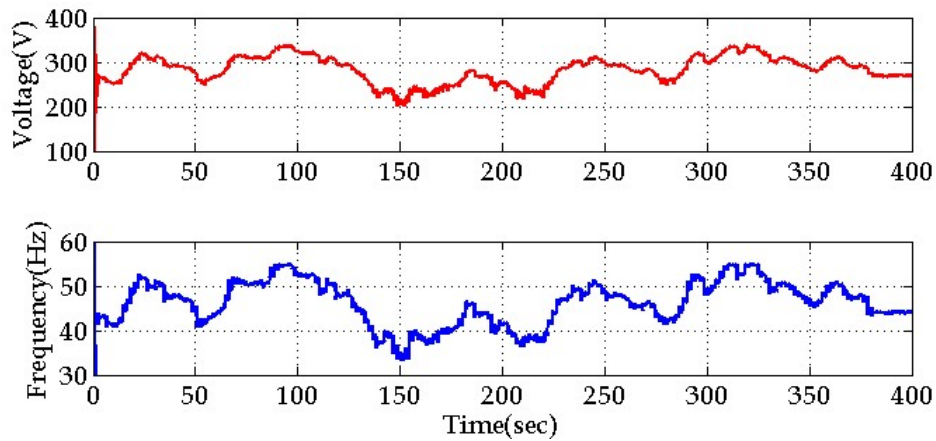
366



367

368 Fig. 20. Variations of wind turbine active power, active pump, and estimated power during wind speed
 369 variation.

370



371

372 Fig. 21. Variations of line RMS voltage and frequency of the SEIG during wind speed variation.

373 5. Experimental Results and Discussion

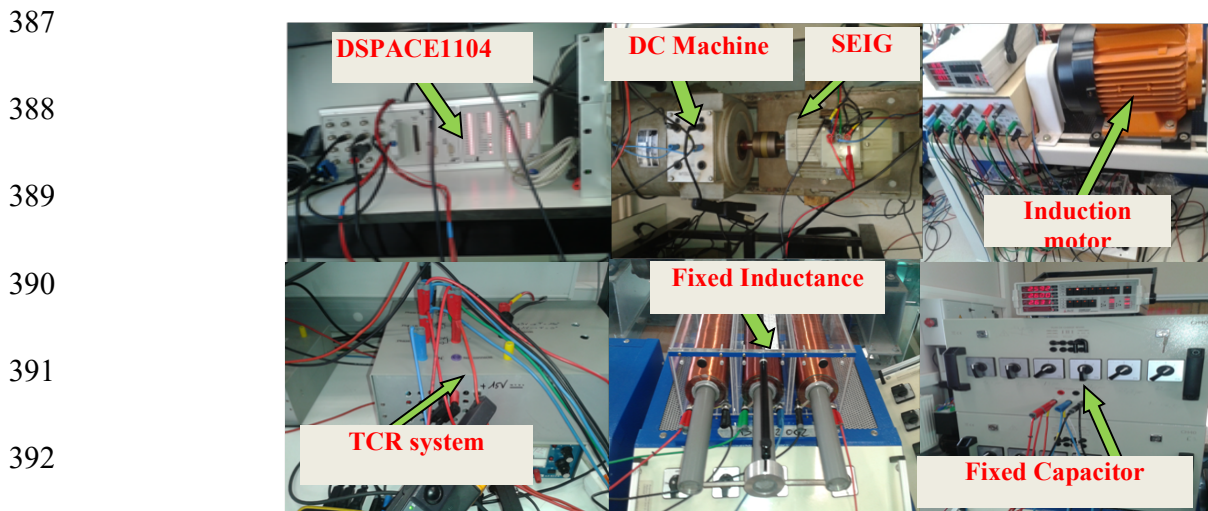
374 5.1. Experimental Setup

375 The configuration of the experimental test bench is shown in Fig. 22. The proposed MPPT algorithm
 376 is implemented using a digital controller based on a dSPACE unit. The system components are:

- 377 - power-controlled DC motor drive which is used to emulate the characteristics of the wind turbine
 378 and to gives P_w at the SEIG shaft.
- 379 - 2[kW] squirrel-cage induction motor which is mechanically coupled to a break to emulate the
 380 centrifugal pump system, a TCR system converter connected in parallel with the SEIG output

381 terminals for the control of the reactive power, and a dSPACE controller board which is
382 interfaced with a PC under Matlab/Simulink.

383 The output signals of the voltage and current transducers are sampled in dSPACE DSP under
384 DS1104-ADC blocks. Low pass filters are used in measuring units to eliminate the unwanted high-
385 frequency noise. The PWM pulses from the dSPACE are sampled under a DS1104-DSP-PWM block to
386 generate standard 10 kHz fixed-frequency PWM pulses.



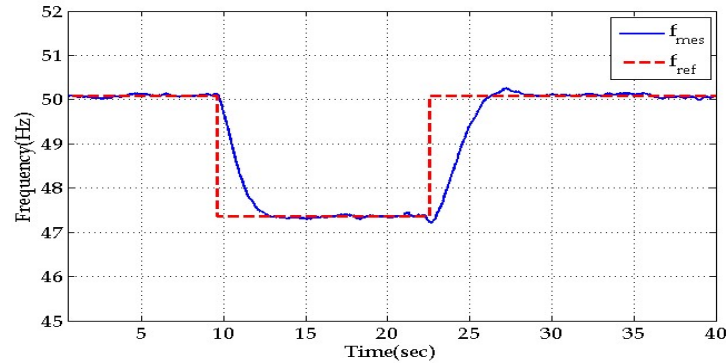
393 Fig. 22. Constituting elements of the experimental test bench.

394 5.2. Experimental Results

395 The performance of the MPPT control strategy was validated experimentally using a laboratory test
396 bench composed of an IG which feeds an IM loaded by a specific break characteristic in order to assure
397 a pump emulator. Different wind speed operating conditions are created by a DC motor which receives
398 a power control in order to assure a constant power P_w at the SEIG shaft making it possible to
399 investigate the dynamic characteristics of a SEIG-Pump system and to find the maximum of the power
400 with the proposed method.

401 Experimental tests were carried out considering two speed profiles applied to the wind turbine, the
402 first considers a decrease and the second an increase of the wind speed turbine. These profiles are used

403 to test the performances of the new proposed PSO MPPT controller algorithm and to analyze the signal
 404 variations. During the tests, a step wind (power) variation is considered. The following tree pictures
 405 (Fig. 23, Fig. 24 Fig. 25) shown the evolution of specific parameters during the decreasing wind speed.
 406 As the frequency is dependent on the rotor speed the step reference is highlighted by the frequency
 407 reference presented in Fig. 23. For experimental induction machines characterized by the parameters
 408 presented in Appendix 1, the frequency 50 Hz corresponds to 13 m/s wind speed and the frequency 47.4
 409 Hz to 12 m/ s wind speed. The transitory time includes the inertia of the SEIG-Pump system and also of
 410 the wind turbine emulator which uses a power control loop.

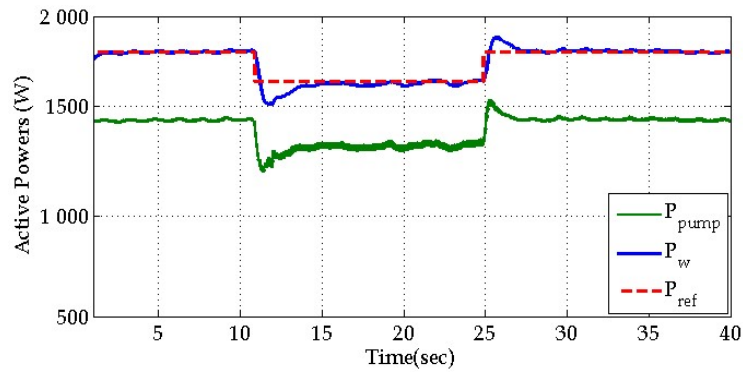


411

412 Fig. 23. Wave forms of reference frequency f_{ref} and SEIG measured frequency f_{mes} for wind speed
 413 switching from $V_w = 13\text{m/s}$ to $V_w = 12\text{ m/s}$ and return to 13 m/s .

414

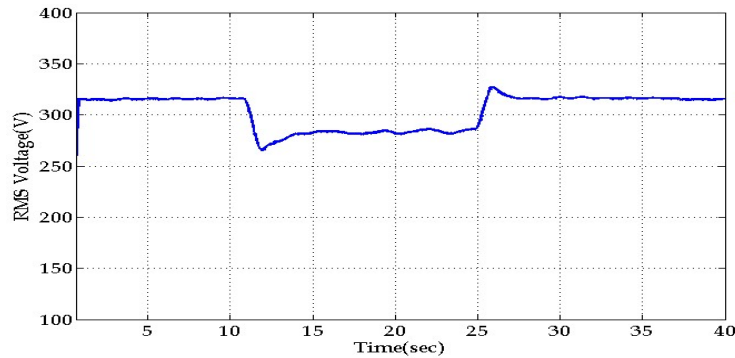
415 The reference power P_{ref} applied at the SEIG, the estimated power obtained from PSO algorithm and
 416 a power consumed by the pump P_{pump} are shown in Fig. 24. For MPP reaching an adjustment of the
 417 SEIG excitation capacitor is applied using a TCR system. We can notice a good power estimation
 418 obtained by the proposed algorithm compared to P_w power reference applied to the PWM converter
 419 (Fig.1). The difference between P_{pump} and P_w corresponds to the DC motor and IG losses.



420

421 Fig. 24 . Wave forms of reference power P_{ref} , estimated power P_w obtained by PSO-MPP algorithm and
 422 the power consumed by the pump P_{pump} for wind speed switching from $V_w = 13\text{m/s}$ to $V_w = 12\text{ m/s}$ and
 423 return to 13 m/s .

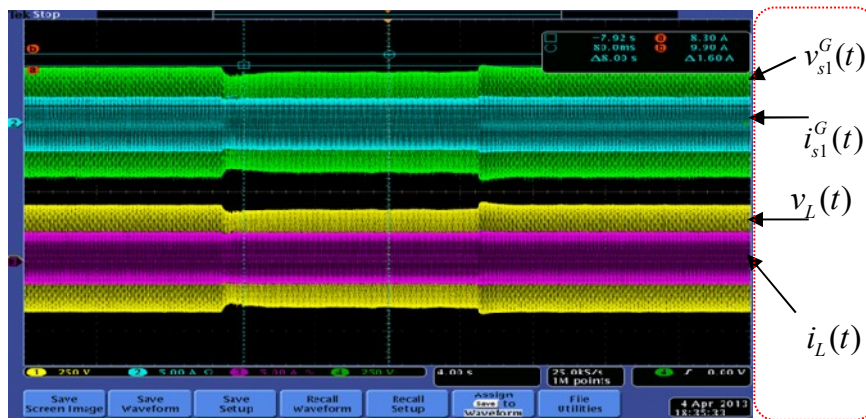
424 The RMS voltage variation measured at the SEIG output is presented in Fig. 25. Here during the
 425 wind variation the voltage changes between 308V at 284V with the low overtaking caused by the wind
 426 power variation (regulation) at the SEIG shaft.



427

428 Fig. 25. Measured phase RMS voltage at the SEIG output for wind speed switching from $V_w = 13\text{m/s}$ to
 429 $V_w = 12\text{ m/s}$ and return to 13 m/s .

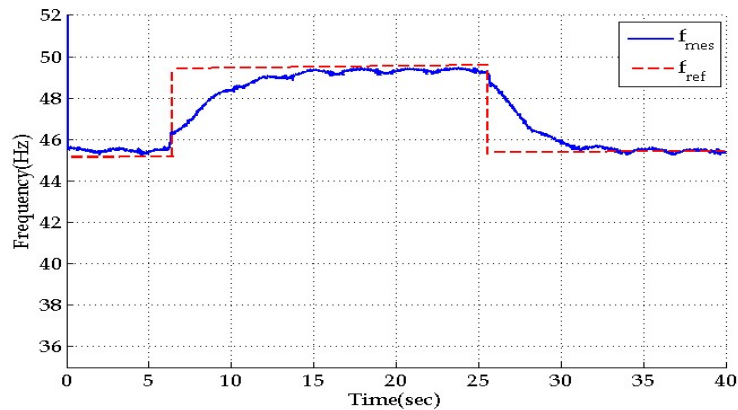
430 For considered speed (power) variation the wave forms of recording signals are presented in Fig. 26.
 431 Here the top recording lines show the voltage and the current measured at the SEIG output and the
 432 bottom lines the voltage and the current measured at the TCR input. We can notice the voltage
 433 decreasing with a very low influence of the currents.



434

435 Fig. 26. Wave forms of recording signals : top lines show voltage and current lines measured at the
 436 SEIG output, bottom lines show voltage and current lines of TCR system for wind speed switching
 437 from $V_w = 13\text{m/s}$ to $V_w = 12\text{ m/s}$ and return to 13 m/s .

438 The following tree pictures show the signal variations (frequency, power, voltage,) in the second
 439 case when the wind speed increases from $V_w = 10\text{m/s}$ to $V_w = 13\text{ m/s}$ and returns to 10 m/s . The
 440 frequency target and the real frequency variations are presented in Fig. 27. We can notice in this case a
 441 frequency value close to the reference with different transitory interval time for increasing and
 442 decreasing of the wind speed.



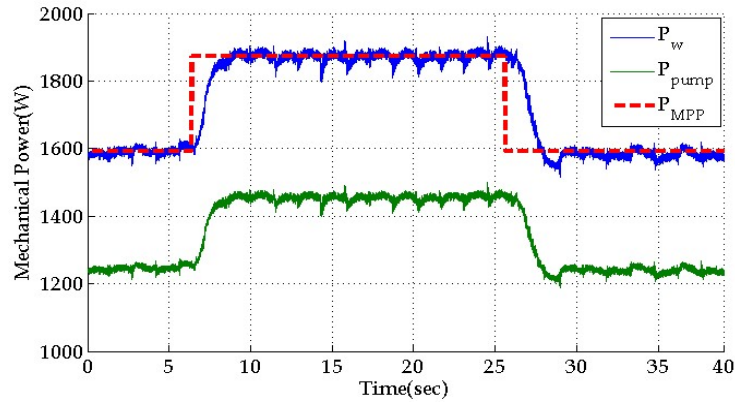
443

444 Fig. 27. Wave forms of reference frequency f_{ref} and SEIG measured frequency f_{mes} for wind speed
 445 switching from $V_w = 10\text{m/s}$ to $V_w = 13\text{ m/s}$ and return to 10 m/s .

446 For this case the power estimation P_{MPP} obtained by the proposed algorithm and the measured power
 447 absorbed by the pump P_{pump} are presented in Fig. 28. The reference power P_{ref} is a step signal changing

448 between 1640W and 1870W. Taking into consideration the DC motor and the IG losses we can notice
 449 the identical variation for P_{pump} and P_{MPP} . The difference during the transitory interval between P_{MPP} and
 450 P_w can be justified by regulation power at the SEIG shaft.

451

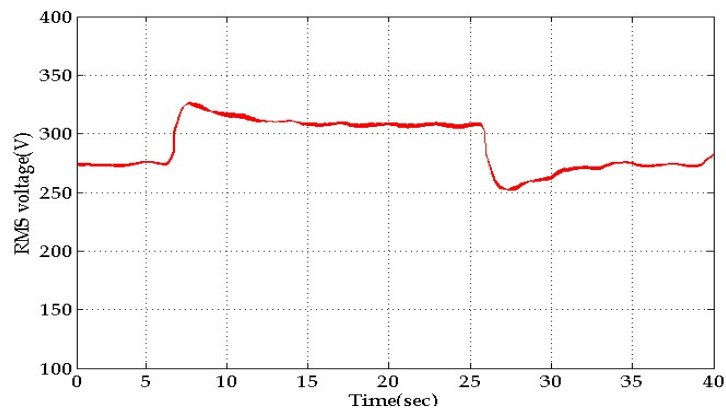


452

453 Fig. 28. Wave forms of reference power P_{ref} , estimated power P_w obtained by PSO algorithm and the
 454 power consumed by the pump P_{pump} from $V_w = 10\text{m/s}$ to $V_w = 13\text{ m/s}$ and return to 10 m/s .

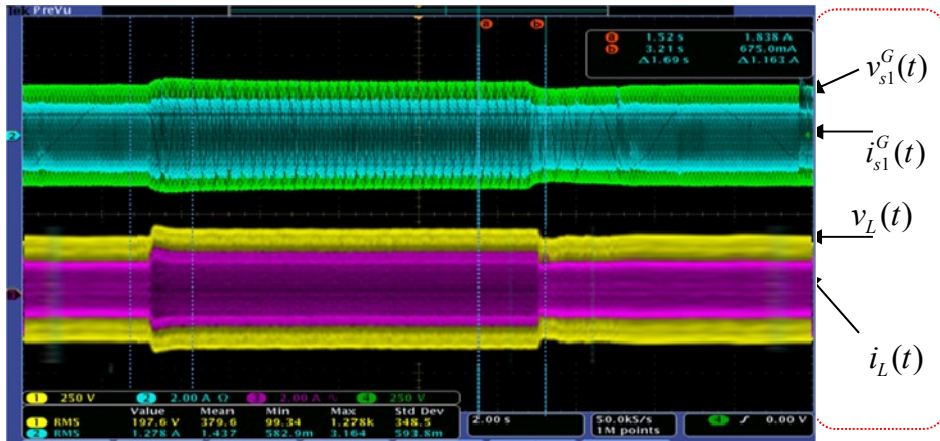
455 The variation of the RMS voltage measured at the SEIG output for wind speed switching from $V_w =$
 456 10m/s to $V_w = 13\text{ m/s}$ and return to 10 m/s is presented in Fig. 29. Here during the steady state the
 457 voltage takes the values 278V and 308V respectively.

458



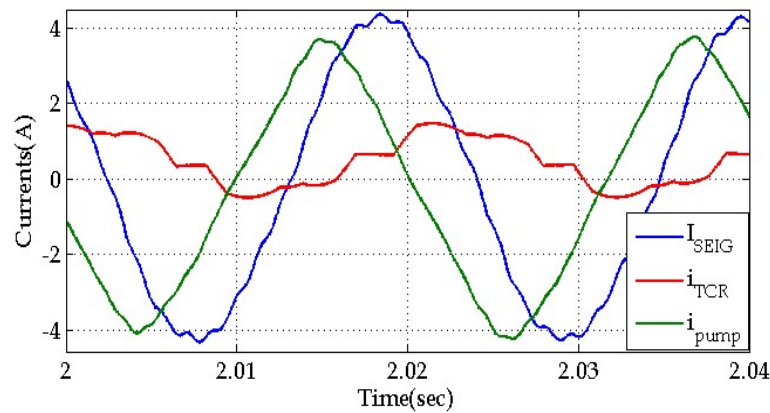
459 Fig. 29. Wave forms of the SEIG RMS voltage for wind speed switching from $V_w = 10\text{m/s}$ to $V_w = 13$
 460 m/s and return to 10 m/s .

461 In the presented figures (Fig. 28 and Fig. 29) the P_{pump} and RMS voltage are reconstituted signals
 462 obtained from instantaneous recording signals of current and voltage measured at the SEIG output and
 463 the P_w is the estimated power obtained by the proposed the PSO algorithm. The wave forms of recorded
 464 signals are presented in Fig. 30.

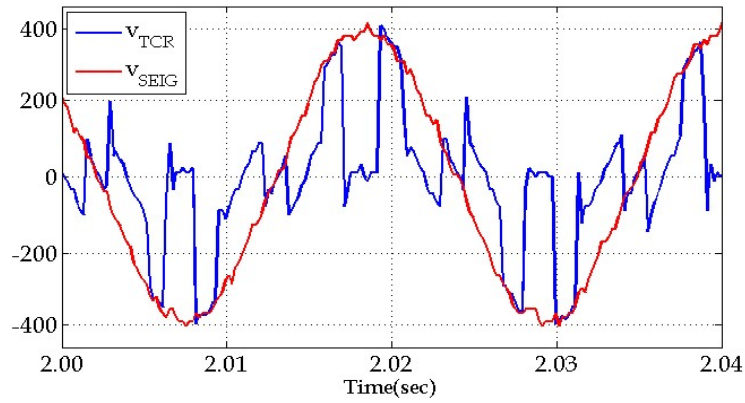


465 Fig. 30 . Wave forms of recording signals : top lines show voltage and current lines measured at the
 466 SEIG output, bottom lines show voltage and current lines of TCR system for wind speed switching
 467 from $V_w = 10\text{m/s}$ to $V_w = 13\text{ m/s}$ and return to 10 m/s .
 468

469 We can observe in Fig. 30 an increasing of the voltage and the current signals (top lines) for $V_w = 13$
 470 m/s and a increase of the I_L current consumed by inductance L_0 in order to decrease the reactive power
 471 in the system. For the second case considered the wave forms of the current and voltage signals are
 472 presented in the following pictures. Fig. 31 gives the signals for wind speed $V_w=10\text{m/s}$ and Fig. 32 for
 473 $V_w=13\text{m/s}$.



474
 475 a) I_{SEIG} current, I_{pump} current and I_{TCR} current



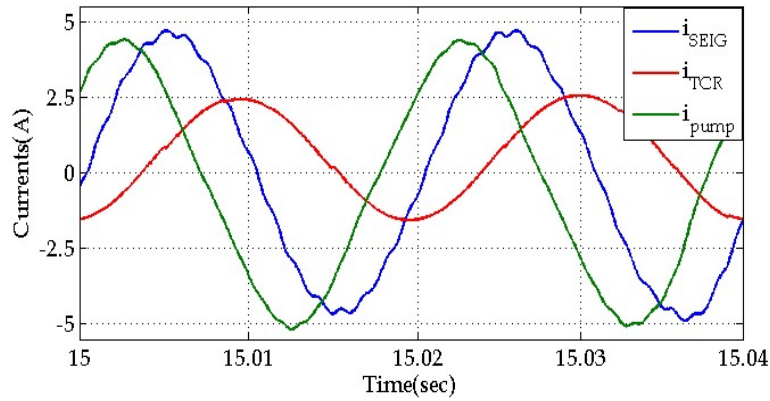
476

477

b) first line voltage of SEIG, and first line voltage of TCR system

478

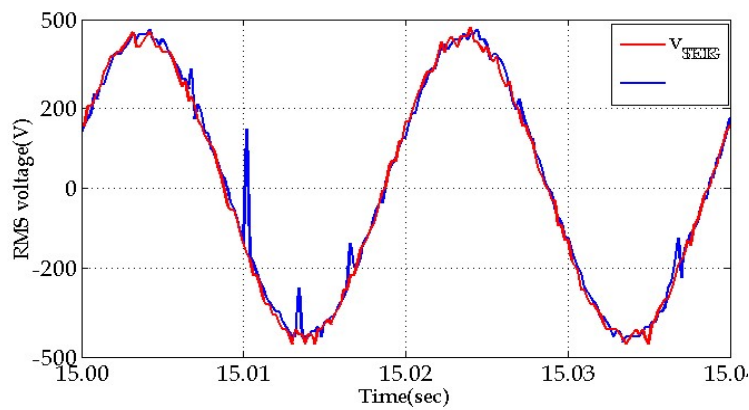
Fig. 31. Zoomed wave forms of a) current and b) voltage for $V_w=10\text{m/s}$ wind speed.



479

480

a) I_{SEIG} current, I_{pump} current and I_{TCR} current



481

482

b) first line voltage of SEIG, and first line voltage of TCR system

483

Fig. 32. Zoomed wave forms of a) current and b) voltage for $V_w=13\text{m/s}$ wind speed.

484 To conclude all steady state analyses results, a summary of the SEIG performance is tabulated in
 485 Table 1.

486 Tab.1 Steady state results

	Simulation Results			Experimental Results		
$V_w(\text{m/s})$	12	10	13	12	10	13
$V_s(\text{V})$	285.5	274.4	303	284	278	308
$f(\text{Hz})$	47	45	50	47.4	45.1	50
$P_{\text{MPPT}}(\text{W})$	1660	1598	1880	1640	1580	1870
$P_{\text{Pump}}(\text{W})$	1352	1250	1462	1335	1247	1460
Losses(W)	308	348	418	305	333	410
η (%)	81.5	78.2	77.7	81.4	78.9	78

487

488 6. Conclusion

489 This paper presents the performance of a Self Excited Induction Generator Pumping system used in
 490 the case of variable wind speed. The system is able to track a maximum power using a generated power
 491 as input. The Maximum Power Point Tracking controller sets the generator to work at the optimal rotor
 492 speed command, which is achieved through a frequency control loop by changing the reactive power.
 493 The proposed system has been implemented in a real-time application, using two Induction Machine
 494 (generator and pump) and a DC motor for emulator of the wind turbine behavior. Simulation and
 495 experimental results show the appropriate behavior of the system.

496 In this paper a new MPPT control algorithm involving PSO technique without use of a rotor speed
 497 sensor is proposed. The wind turbine in operation delivers the maximum mechanical output power for a
 498 given wind velocity. It is considered that the slip of the SEIG is very small. Therefore, when operating

499 the induction generator with wide rotor speeds achieving MPPT, the frequency of the SEIG is controlled
500 to reach the optimal rotor speed ω_{ropt} .

501 A proposed PSO-MPPT based algorithm is presented in this work as a case study. The advantage of
502 the proposed method is that it does not require the knowledge of wind speed, air density or turbine
503 parameters. The MPPT controller generates at its output the optimum capacitor command C_{opt} for rotor
504 speed control loop using only the instantaneous active power as input signal.

505 From, the analyses results, the PSO based MPPT has been proved to be useful in tracking the
506 maximum power point and it is able to respond to the changes of wind speed and power coefficients.

507 However, the global time for tracking of the MPP is dependent by the global inertia of the system
508 and SEIG parameters and can take few second time delay.

509 Nomenclature

Variable	Designation	Variable	Designation
A	Area swept by blades	l_s^G and l_s^M	Leakage inductance of the stator winding of IG and IM
B	Fundamental frequency susceptance		
C_0	Big fixed capacitor	l_r^G and l_r^M	Leakage inductance of the rotor copper of IG and IM
C_{min} and C_{max}	Low bound and upper bound values of the optimal capacitor	L_m^G and L_m^M	Magnetizing inductances of the IG and IM
C_j^k	j^{th} capacitor at iteration k	L_0	Big fixed self inductance.
C_{Gbest}	Global best capacitor of each group	N_p	Number of particles
C_{opt}	Optimal capacitor	p	Pair of poles
C_p	Power coefficient of the wind turbine	P_{jref}^k	j^{th} reference mechanical power at iteration k
C_{pbest}^k	Best capacitor of j^{th} particle until iteration k	P_{wj}^k	j^{th} mechanical power at iteration k
f_j^k	j^{th} frequency at iteration k	P_w, P_{pump}	Mechanical powers of the wind turbine respectively the pump
Fit, Fit_{opt}	Fitness function and Optimal Fitness function	P_{MPP}	Maximum power extracted from the wind turbine
G_{best}	Global best particles	P_{best}	Local best particles
j	Index of particles	Q_{TCR}, Q_{C0} and Q_L	Reactive powers of the TCR system, the capacitor and the inductance
J	Global inertia of system.	R_w	Radius of the wind turbine blade

k	k^{th} iteration	$rand$	Random numbers which are uniformly distributed in interval [0, 1]
k_n	Torque-rotor speed coefficient	U_{DC} and I_{DC}	DC voltage and current
V_j^k	Velocity of j^{th} particles at iteration k	δ_1 and δ_2	Positive constants
V_w	Wind speed	λ_{opt}	Optimum Tip Speed Ratio.
V_s	RMS of the SEIG terminal voltage	λ	Tip Speed Ratio.
X_j^k	Position of j^{th} particles at iteration k	μ	Momentum or inertia
β	Blade pitch angle	ω_r^G and ω_r^M	Electrical rotor speed of IG and IM
Γ_{em}^G and Γ_{em}^M	Electromagnetic torque developed by the IG and IM	ω_{rj}^k	j^{th} rotor speed at iteration k
Γ_f	Friction torque	ω_{ropt}	Optimum rotor speed
Γ_w	Mechanical torque of the wind turbine	ω_{ropt}^G	Optimal rotor speed

510

511 Appendix 1

512 The considered induction generator is characterized by:

513 $380/660V$, $7.3/4.2A$, 1420 rpm , $f = 50\text{Hz}$, $\cos(\varphi) = 0.8$, $p = 2$, $R_s^G = 8.66\ \Omega$, $R_r^G = 3\ \Omega$,
514 $l_s^G = 24.24\text{ mH}$, $l_r^G = 36.3\text{ mH}$, $L_m^G = 534\text{ mH}$, $L_s^G = 558.24\text{ mH}$, $L_r^G = 570.3\text{ mH}$, $\Gamma_f = 1.3\text{N.m}$

515 The considered induction motor is characterized by:

516 $380/660V$, $5.2/3A$, 1420 rpm , $f = 50\text{Hz}$, $\cos(\varphi) = 0.89$, $p = 2$, $r_s^M = 3.7\ \Omega$, $r_r^M = 2.72\ \Omega$,
517 $l_s^M = 20.78\text{ mH}$, $l_r^M = 14.8\text{ mH}$, $L_m^M = 436.6\text{ mH}$, $L_s^M = 457.38\text{ mH}$, $L_r^M = 451.4\text{ mH}$,

518 References

519 [1] R. C. Bansal, "Three-phase Self-Excited Induction Generators: an overview," 16th national power
520 systems conference, IEEE transactions on Energy Conversion, vol. 20, no. 2, June 2005, pp. 292-
521 299.

522 [2] D. Halamay, T. Brekken, A. Simmons, and S. McArthur, "Reserve Requirement Impacts of Large-
523 Scale Integration of Wind, Solar and Ocean Wave Power Generation, " IEEE Transactions on
524 Sustainable Energy, no 2, Dec 2011, pp. 321-328.

- 525 [3] L. Wang, and Z. Chen, "Stability Analysis of a Wave-Energy Conversion System Containing a Grid-
526 Connected Induction Generator Driven by a Wells Turbine," IEEE Transactions on Energy
527 Conversion, no 25, Jun 2010, pp. 555-563.
- 528 [4] G. Ofualagba, E.U.Ubeku, "The analysis and modelling of a self-excited induction generator driven
529 by a variable speed wind turbine," Federal University of Petroleum Resources, Effurun, Nigeria. In
530 Book –Fundamentals and Advanced Topics in Wind Power, Vol. 2, June 2011, ISBN 978-953-307-
531 508-2.
- 532 [5] I. Boldea, and S. Nasar, "The induction machine handbook. 1st ed. Boca Raton » USA: CRC Press;
533 2002.
- 534 [6] R. C. Bansal, T. S. Bhatti, and D. P. Kothari, "A bibliographical survey on induction generators for
535 application of nonconventional energy systems," IEEE Trans. Energy Convers., Vol. 18, no. 3,
536 September 2003, pp. 433–439.
- 537 [7] Jayanta K. Chatterjee, "Analysis Voltage and Frequency Control of a Stand Alone Brushless Wind
538 Electric Generation Using Generalized Impedance Controller," IEEE Trans. Energy Convers., vol.
539 23, no. 2, June 2008, pp. 632-641.
- 540 [8] J.F. Brudny, R. Pusca, and H. Roisse, "Wind turbines using self-excited three-phase induction
541 generators: an innovative solution for voltage-frequency control," Eur. Phys. J. Appl. Phys. 43,
542 2008, pp. 173–187
- 543 [9] Bhim Singh, S. S. Murthy, Raja Sekhara , "STATCOM-Based Controller for a Three-Phase SEIG
544 Feeding Single-Phase Loads" IEEE Trans. Energy Convers., Vol. 29, no. 2, June 2014, pp. 320-331.
- 545 [10] S.S. Murthy, Bhim Singh, V. Sandeep, "An analytical performance comparison of two winding
546 and three winding single phase SEIG", Electric Power Systems Research, Vol. 107, February 2014,
547 pp. 36–44.

- 548 [11] Cosmas .U. Ogbuka, Member, IAENG and Marcel. U. Agu, MIEEEE, “A Modified Approach to
549 Induction Motor Stator Voltage and Frequency Control,” Proceedings of the World Congress on
550 Engineering, 2011, Vol II, WCE 2011, 6 – 8 July 2011, London, U.K. pp. 978-988.
- 551 [12] Jayanta K. Chatterjee, “Analysis Voltage and Frequency Control of a Stand Alone Brushless
552 Wind Electric Generation Using Generalized Impedance Controller,” IEEE Trans. Energy Convers.,
553 vol. 23, no. 2, June 2008, pp. 632-641.
- 554 [13] Manel Ouali, Mohamed Ben Ali Kamoun, Maher Chaabene “ Investigation on the Excitation
555 Capacitor for a Wind Pumping Plant Using Induction Generator,” Smart Grid and Renewable
556 Energy, 2011, 2, pp. 116-125.
- 557 [14] Messaoud Makhlouf, Feyrouz Messai and Hocine Benalla “Vectorial Command Of Induction
558 Motor Pumping System Supplied By A Photovoltaic Generator,” Journal of Electrical Engineering,
559 Vol. 62, No. 1, 2011, pp. 3–10.
- 560 [15] V. Agarwal, R.K. Aggarwal, P. Patidar, C. Patki, A novel scheme for rapid tracking of maximum
561 power point in wind energy generation systems, IEEE Trans. Energy Convers. Vol. 25 , Jun 2010,
562 pp. 228-236.
- 563 [16] T. Ouchbel , Smail Zouggar, M.L. Elhafyani, M. Seddik, M. Oukili and A. Aziz “Power
564 maximization of an asynchronous wind turbine with a variable speed feeding a centrifugal pump,”
565 Energy Conversion and Management, Vol. 78, February 2014, pp. 976–984.
- 566 [17] David Laraa, Gabriel Merinoa, Lautaro Salazar, “Power converter with maximum power point
567 tracking MPPT for small wind-electric pumping systems,” Energy Conversion and Management, V.
568 97, June 2015, pp. 53–62.
- 569 [18] René Aubréca, b, François Augera, Michel Macéc, Luc Lorona, “Design of an efficient small
570 wind-energy conversion system with an adaptive sensorless MPPT strategy”, Renewable Energy,
571 Vol. 86, February 2016, pp. 280–291.

- 572 [19] Dalala Z. M., Zahid Z.U., Wensong Y.U., Younghoon Cho, Gih-Sheng Lai, "Design and
573 Analysis of an MPPT Technique for Small-Scale Wind Energy Conversion Systems", IEEE Trans.
574 Energy Convers, Vol. 28, No. 3, September 2013, pp 756-767.
- 575 [20] Cong-Hui Huang, " Modified Neural Network for Dynamic Control and Operation of a Hybrid
576 Generation Systems, "Journal of Applied Research and Technology, Vol. 12, December 2014, pp.
577 1154-1164.
- 578 [21] David Lara, Gabriel Merinoa, Lautaro Salazar, "Power converter with maximum power point
579 tracking MPPT for small wind-electric pumping systems", Energy Conversion and Management, V.
580 97, June 2015, pp. 53–62.
- 581 [22] Samira Chekkal "Fuzzy logic control strategy of wind generator based on the dual-stator
582 induction generator", International Journal of Electrical Power & Energy Systems, Vol. 59, July
583 2014, pp. 166–175.
- 584 [23] A. Betz, Das Maximum der theoretisch möglichen Ausnutzung des Windes durch Windmotoren,
585 Gesamte Turbinenwesen , Vol. 17, Jun 1920, pp. 307–309.
- 586 [24] J.G. Slootweg, S.W.H. de Haan, H. Polinder, W.L. Kling, "General model for representing
587 variable speed wind turbines in power system dynamics simulations", IEEE Trans. Power Syst. Vol.
588 18 , Decmber 2003, pp. 144-151.
- 589 [25] Ouchbel T, Zouggar S, Sedik M, Oukili M, Elhafyani M, et al. Control of the output voltage of
590 asynchronous wind turbine with variable speed using a static VAR compensator (SVC) smart
591 innovation, systems and technologies. Sustain Energy Build Part 1 , Vol. 12, March 2012, pp 17–30,
- 592 [26] Shi, Y., Eberhart, R.: "Empirical study of particle swarm optimization", Proceedings of the IEEE
593 Congress on Evolutionary Computation, Piscataway, NJ, IEEE Press , Jun 1999, pp 1945–1950.

- 594 [27] Ali Ajami and Mehdi Armaghan, "Application of Multi-Objective PSO Algorithm for Power
595 System Stability Enhancement by Means of SSSC," International Journal of Computer and Electrical
596 Engineering, Vol. 2, No. 5, October 2010, pp. 838-845.
- 597 [28] Sabine Helwig, Frank Neumann, and Rolf Wanka, "Particle Swarm Optimization with Velocity
598 Adaptation," International Conference on Adaptive and Intelligent Systems. 24-25 September 2009,
599 Las Vegas, pp.146-151.

600